RESEARCH ARTICLE | AUGUST 16 2022

Gas–surface interactions in a large-scale inductively coupled plasma wind tunnel investigated by emission/absorption spectroscopy

Sihan Fang (方思晗); Xin Lin (林鑫) ✉; Hui Zeng (曾徽); ... et. al

Physics of Fluids 34, 082113 (2022)
https://doi.org/10.1063/5.0102274

Physics of Fluids ARTICLE scitation.org/journal/phf

Gas–surface interactions in a large-scale inductively coupled plasma wind tunnel investigated by emission/absorption spectroscopy

Cite as: Phys. Fluids **34**, 082113 (2022); doi: 10.1063/5.0102274
Submitted: 8 June 2022 · Accepted: 22 July 2022 ·
Published Online: 16 August 2022

Sihan Fang (方思晗),[1,2] Xin Lin (林鑫),[1,a)] Hui Zeng (曾徽),[3] Xingying Zhu (朱兴营),[3] Fa Zhou (周法),[3] Junna Yang (杨俊娜),[1,2] Fei Li (李飞),[1] Dongbin Ou (欧东斌),[3] and Xilong Yu (余西龙)[1,2]

AFFILIATIONS

[1]State Key Laboratory of High Temperature Gas Dynamics, Institute of Mechanics, Chinese Academy of Sciences, Beijing 100190, China
[2]School of Engineering Science, University of Chinese Academy of Sciences, Beijing 100049, China
[3]China Academy of Aerospace Aerodynamics, Beijing Key Laboratory of Arc Plasma Application Equipment, Beijing 100074, China

[a)]**Author to whom correspondence should be addressed:** linxin_bit@imech.ac.cn

ABSTRACT

Precise prediction of aerothermal loads is significantly limited by the unclear interactions between the thermal protection system surface and the surrounding high-enthalpy gas. To address this, we propose an optical diagnostic method based on optical emission spectroscopy and laser absorption spectroscopy to investigate the gas–surface interactions within the boundary layer. Experiments are conducted in an air plasma flow produced by the 1.2 MW inductively coupled plasma wind tunnel at the China Academy of Aerospace Aerodynamics with an enthalpy of 20 MJ/kg and a heating time of 100 s. The cylindrical samples made of pure silicon carbide are tested, and quartz samples with the same exposed geometry are tested in parallel as a reference material. The optical emission spectroscopy system has four spectrometers to cover the wide wavelength range of 200–1100 nm, providing qualitative, spatially, and spectrally resolved measurements of the multi-species radiative emission adjacent to the sample surface. Laser absorption spectroscopy is deployed at different axial locations to quantify the number density and translational temperature of OI (3s5S) with a 500 Hz scanning rate and 200 kHz acquisition rate. Additionally, the surface temperature of each sample is detected by an infrared pyrometer. Scanning electron microscopy and energy dispersive spectrometry are performed before and after the plasma heating. Our measurement results provide valuable information on surface reaction pathways and catalytic recombination effects on atomic oxygen number density distributions. Finally, these self-consistent results show that the proposed method is reliable to deeply investigate gas–surface interactions within boundary layer in harsh aerothermal environment.

I. INTRODUCTION

During an atmospheric entry, a strong detached bow shock is formed ahead of the space vehicle, and the high-temperature air between the bow shock wave and the thermal protection system (TPS) surface is partially dissociated into atoms.[1–6] As the dissociated atoms move toward the vehicle, the temperature decreases rapidly from the boundary layer edge to the TPS surface, but the gas mixture could not fully equilibrate in this short distance within the thermal boundary layer.[7–9] Under these nonequilibrium states, complex interactions between the dissociated gas and TPS surface occur within the boundary layer. Catalytic recombination between dissociated atoms is one of the important processes among gas–surface interactions that significantly enhance aerothermal heating.[10–13] However, the TPS design remains overly conservative because considerable uncertainty remains in predicting thermochemical ablation rates at high surface temperatures. This adds unnecessary payload weight and reduces payload opportunities.[14] It is noteworthy that atomic number density distributions on a TPS surface closely relate to the recombination process,[15] and radiative properties are important because they reflect species components in the reactive flow.[16] Therefore, it is important to quantify the atomic number density and investigate dynamic spectral characteristics adjacent to the TPS surface to gain a deeper

understanding of the cumulative exothermic nature of surface catalytic recombination.[12,17]

Past experiments on surface catalytic recombination have mainly used two approaches. The first is based on *heat flux measurements* and the second on *concentration measurements*.[18] The *heat flux measurements* approach was based on Goulard's theory of stagnation point heat transfer, whereby the recombination coefficient is obtained by comparing the measured heat flux on the investigated material with that of a reference material (generally CuO, considered fully catalytic),[19] or by extracting the recombination heat flux from the total heat flux with an iterative procedure.[20] Such an approach is generally used in high-enthalpy ground facilities such as arc-jet or inductively coupled plasma (ICP) wind tunnels, which are good at reproducing realistic flow conditions.[21] However, the measurement accuracy strongly depends on the recombination coefficient set for the reference material.[19,22] This approach gives the bulk effect of the total augmented heat transfer,[7] but it is still the unresolved product of complex physico-chemical mechanisms. As for the *concentration measurements* approach, actinometry and laser-induced fluorescence (LIF) are two main methodologies. Based on mass balance between the arriving diffusive flux and the recombination consumption rate, both methodologies aim to inform axial distributions in number densities.[7,23] However, quantitative determination of number density is limited for various reasons. In actinometry methodology, compensating the variations in electronic density requires dividing the emission intensity of the targeted atom by that of an inert gas.[24] This enables the relative number density to be deduced, assuming that the targeted atom and the inert gas have similar energy thresholds.[25] In LIF methodology, quantifying atomic number density requires complicated calibrations of signal intensity and measurements of fluorescence lifetime, beam diameter, and detection efficiency,[7,26] which are difficult to obtain in practical reactive flows.[27] Moreover, the laser equipment of LIF is typically not fiber coupled and requires a close proximity to the test platform. Finally, LIF requires bulky light sources and sophisticated laser equipment,[27] and its signals usually suffer from collisional quenching. Owing to these limitations of actinometry and LIF, *concentration measurements* approach is generally used in plasma facilities with relatively low enthalpy, which differs greatly from the severe aerothermal environments in real flight.[28,29]

For thermochemistry research in reactive plasmas, optical emission spectroscopy (OES) is a nonintrusive diagnostic technology that has been widely used to study chemical reactions and analyze radiation characteristics.[30–32] With the advantages of being sensitive and convenient,[33] OES allows simultaneous detection of emission intensities of multiple species in a wide wavelength range, providing valuable information on chemical reactions. Laser absorption spectroscopy (LAS) is a powerful technology to access the ground state of atoms and molecules for flow characterization, allowing diagnosis with high fidelity, fast response, robustness, and compactness.[34,35] Over the past two decades, LAS has penetrated into many areas such as atmospheric monitoring,[36] combustion diagnostics,[37,38] and plasma characterization.[39,40] Considering the qualitative multiple-species sensing of OES and quantitative species-specific nature of LAS, both techniques were combined in our work.

This paper presents the application of OES and LAS diagnostic technique regarding gas–surface interactions in high-enthalpy air plasma. Experiments are conducted in a 1.2 MW ICP wind tunnel at the China Academy of Aerospace Aerodynamics (CAAA) with an enthalpy of 20 MJ/kg and 100 s of heating time. Characteristic TPS material silicon carbide (SiC) is tested together with quartz as a reference material. LAS system is employed at different axial locations to quantify the number density and translational temperature of OI ($3s^5S$) as well as their variations. OES detection of characteristic products is used to distinguish between competing mechanisms in reaction zone. Additionally, surface temperatures are detected by a monochromatic infrared optical pyrometer. Scanning electron microscope (SEM) and energy dispersive spectrometry (EDS) are used to evaluate changes in the morphology and composition due to plasma exposure. Based on these results, analysis is made between SiC and quartz materials to figure out surface reaction pathways. Furthermore, relations between atomic oxygen densities and catalytic property are discussed.

II. LASER ABSORPTION SPECTROSCOPY

A. Theory

The basic principle of LAS is briefly outlined here. For diagnosis in high-temperature plasmas, LAS is mainly dominated by the Beer–Lambert law, which describes the relationship between incident (I_0) and transmitted (I_t) intensity of a monochromatic laser beam propagating through a uniform absorbing medium[41–43]

$$k_\nu L = \ln\left(I_0/I_t\right)_\nu, \tag{1}$$

where L is the absorption length, and k_ν is the absorption coefficient at the frequency ν (s^{-1}), which can be expressed as

$$k_\nu = S_{lu} n_l \phi_\nu, \tag{2}$$

where

$$S_{lu} = \left(\frac{\lambda_0}{8\pi c}\right) A_{ul} \frac{g_u}{g_l}\left[1 - \exp\left(-\frac{hc}{\lambda_0 k_B T_{ex}}\right)\right]. \tag{3}$$

Here, S_{lu} [$cm^{-1}/(mol\ cm^{-2})$] is the line strength of the transition, n_l (cm^{-3}) is the lower-state number density of the targeted species, c is the velocity of light, h is the Planck constant, k_B is the Boltzmann constant, and T_{ex} is the electronic excitation temperature that describes the ratio of the number densities at the lower and upper states.[41] In this study, the term $hc/\lambda_0 k_B$ of atomic oxygen line at 777.19 nm is about 20 000 K,[44] which is much lower than T_{ex}. Thus, the exponential term in Eq. (3) is relatively insensitive to changes in T_{ex} in the temperature range of interest,[42,45] and Eq. (3) can be approximated as

$$S_{lu} = \left(\frac{\lambda_0}{8\pi c}\right) A_{ul} \frac{g_u}{g_l}. \tag{4}$$

Because the line shape function ϕ_ν follows the relation

$$\int \phi_\nu d\nu \equiv 1. \tag{5}$$

The lower-state number density of the species n_l can be deduced from the integrated absorbance A_{int} based on Eqs. (2)–(5)

$$n_l = \frac{A_{\mathrm{int}}}{\lambda_0 L (g_u/g_l)(A_{ul}/8\pi c)} = \frac{\int k_\nu d\nu}{\lambda_0 (g_u/g_l)(A_{ul}/8\pi c)}. \tag{6}$$

In our experimental conditions, Doppler broadening is dominant compared with other broadenings such as natural, pressure, and Stark

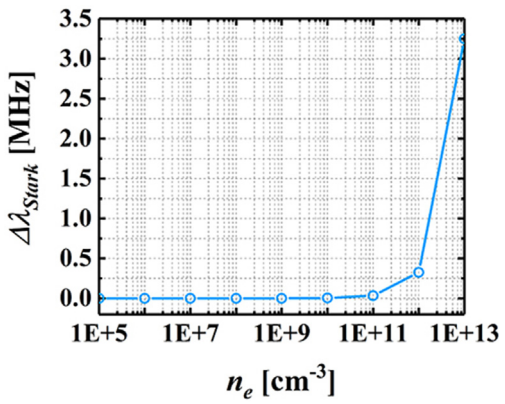

FIG. 1. Stark broadening variations with electron density at $T_e = 10\,000$ K.

broadening (discussed below). Hence, the translational temperature of atomic oxygen T_{tr} is deduced from the Doppler width $\Delta\nu_D$ as follows:[46–49]

$$\Delta\nu_D = 7.162\,3 \times 10^{-7}\nu_0\sqrt{T_{tr}/M}, \tag{7}$$

where ν_0 (cm^{-1}) is the central wavenumber of the transition, and M is the atomic mass.

Generally, absorption line shape is broadened by various physical mechanisms and is assumed as a Voigt profile that includes Doppler broadening and pressure broadening.[47,49] For the expected pressure (approximately 1 kPa) and temperature (approximately 5000 K) in our experiments, the pressure broadening is estimated to be two orders of magnitude smaller than the Doppler broadening.[50] Therefore, pressure broadening can be neglected. Stark broadening, originating from Coulomb interactions between the radiator and charged particles in the plasma, monotonically increases with electron density.[51] This broadening type should be analyzed in our plasma testing environment. The line shape of Stark broadening is the Lorentzian type profile and is expressed as[42,43]

$$\Delta\lambda_{Stark} = 2 \times \left[1 + 1.75 \times 10^{-4} n_e^{1/4}\alpha \times \left(1 - 0.068 n_e^{1/6} T_e^{-1/2}\right)\right] \times 10^{-16}\omega n_e, \tag{8}$$

where n_e is the electron density, T_e is the electron temperature, α is the ion-broadening parameter, and ω is the electron impact parameter. When the electron temperature is 10 000 K, the Stark broadening of atomic oxygen at 777.19 nm shows an upward trend with electron density in the range of 10^5–10^{13} cm^{-3} (Fig. 1). Under our experimental conditions, Doppler broadening is estimated to be approximately 5 GHz according to Eq. (7), which is three orders of magnitude higher than Stark broadening at n_e of 10^{13} cm^{-3}. This shows that the Stark broadening is insignificant compared with Doppler broadening in our experimental conditions. Therefore, the Doppler broadening is considered and other broadenings are neglected.

B. Line selection

The Chemical Equilibrium with Applications (CEA) code was used to simulate the species composition of the air plasma in entry conditions. Figure 2 shows the temperature-dependent (4000–9000 K) mole fraction of the neutral and charged species at pressures of 2 and 8 atm. It is noteworthy that nearly all of the O_2 is dissociated into O,[41] and O becomes one of the major constituents in the dissociated gas in the temperature range of interest. Owing to its highly chemically reactive behavior,[15,52,53] atomic oxygen strongly influences the TPS design mainly through catalytic recombination and oxidation processes.[15] Figure 3 plots the simplified energy-level diagram of atomic oxygen.[41] Absorption line of the OI transition from $3s^5S_2$ to $3p^5P_3$ at the wavelength of 777.19 nm was chosen due to the following reasons. Unlike the ground state, the electronic excited lower state of the transitions near 777 nm is in the visible-near-infrared region, which can be monitored by commercially available diode lasers. Additionally, this metastable state is extremely temperature-sensitive and well isolated from other species in the plasma.[41] Although the upper energy level (^{5}P1;2;3) of the 777 nm lines is a degenerate level (Fig. 3), the spacing of the split upper levels is sufficient enough to resolve a single triplet

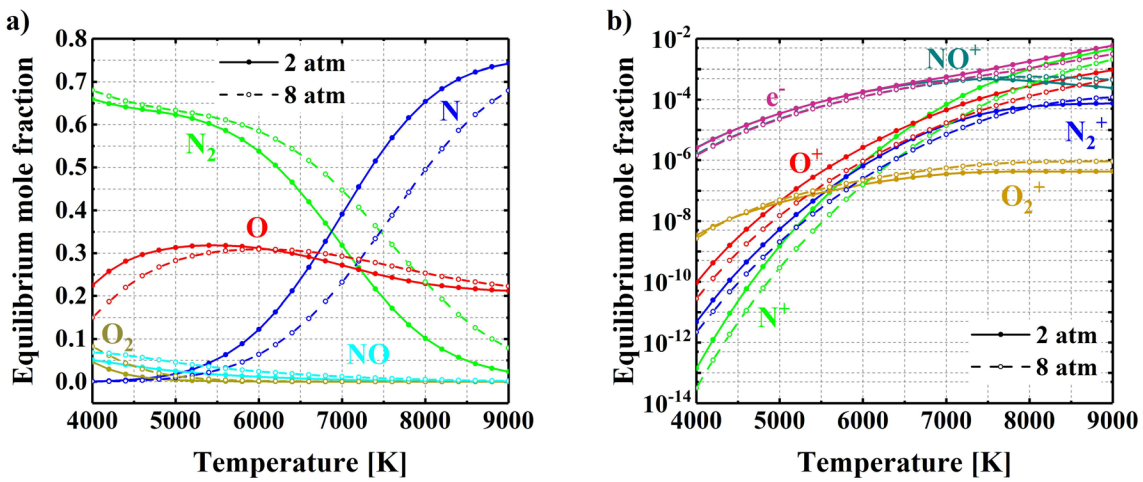

FIG. 2. CEA results: mole fractions of (a) neutral and (b) charged species in dry air at 2 atm (solid line and filled circles) and 8 atm (dashed line and open circles).

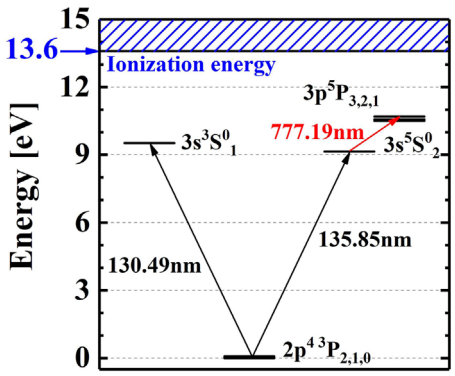

FIG. 3. Simplified energy diagram of atomic oxygen.

component at 777.19 nm.[43] Despite the difference between the profile of ground state and metastable state, the detected metastable state still depicts a thermochemical process.[50] Table I lists the important parameters of the central wavelength λ_0, lower-state energy E_l, upper-state energy E_u, lower-state degeneracy g_l, upper-state degeneracy g_u, and Einstein coefficient A_{ul} of the transition near 777.19 nm.

TABLE I. Transition parameters of atomic oxygen at 777.19 nm.

Transition	λ_0 (nm)	E_l (Ev)	E_u (eV)	g_l	g_u	A_{ul} (10^7 s^{-1})
OI ($3s^5S$ $3p^5P$)	777.19	9.146	10.741	5	7	3.69

III. EXPERIMENTAL SETUP

A. 1.2 MW inductively coupled plasma wind tunnel

An ICP wind tunnel has the advantages of long test time (up to tens of minutes) and high purity flow, which make it ideal for investigating material thermochemistry and gas–surface interactions.[54,55] The experiments were conducted in the 1.2 MW ICP wind tunnel at CAAA. Figure 4 is the schematic of the experimental setup. The wind tunnel consists of an ICP coil, a convergent-divergent supersonic nozzle, a test chamber, and a vacuum system. The plasma generated by the coil was expanded into the test chamber through a hypersonic nozzle and finally extracted by the vacuum system.

In our experiments, standard air (79% N_2 and 21% O_2) was fed into the ICP generator at mass flow rate of 12.84 g/s, providing high-enthalpy plasma flows of 20 MJ/kg. Each sample was tested more than five times to ensure the reliability and repeatability. As the plasma reached a steady state, the test sample was pushed into the flow for an exposure time of 92 s. The ICP tunnel was then shut off after the

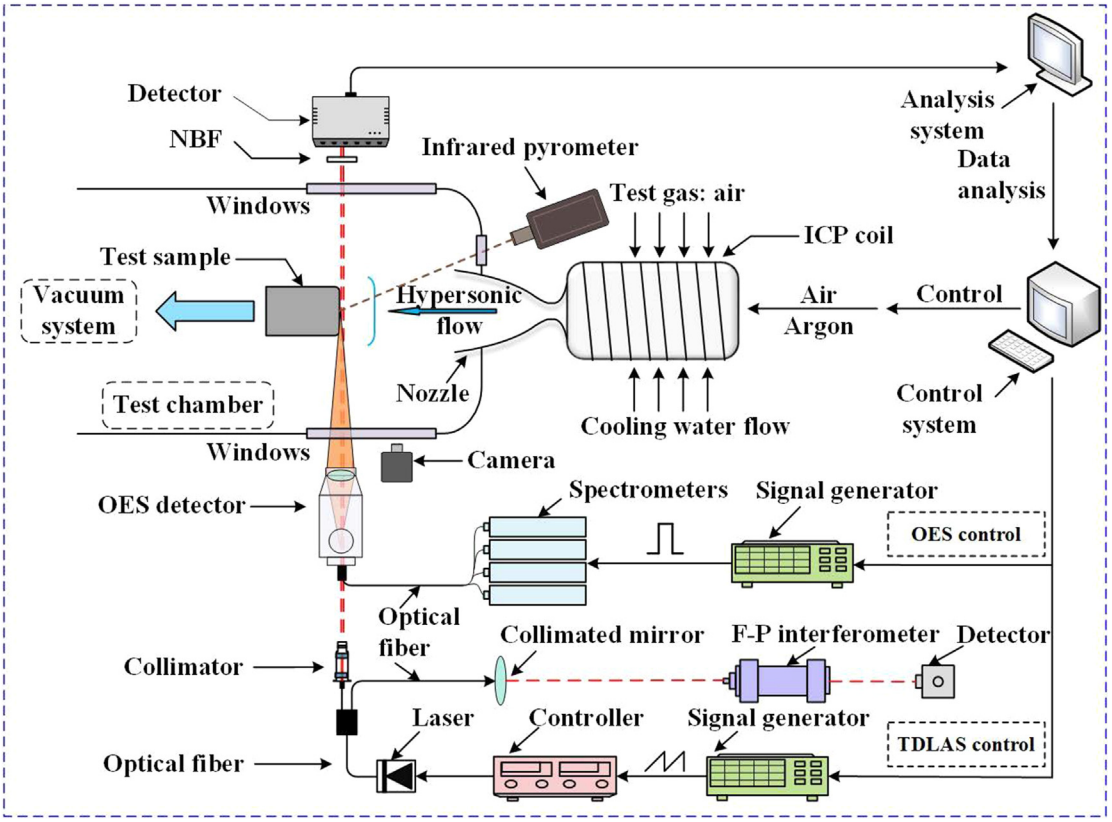

FIG. 4. Schematic image of experimental system.

sample was dragged out of the plasma. A water-cooled Pitot probe was also inserted into the copper probe to perform stagnation pressure measurements.

A monochromatic optical pyrometer (FLUKE Endurance Series, E1MH-F2-L-0-0), operating at 540–3000 °C, monitored the front surface temperature of the tested samples. The output is related to the emissivity (set to 0.9) and transmissivity (set to 1.0) if the targeted surface satisfies the graybody assumption within the operation range.[3] Calibrations of the pyrometer are performed before the experiments using a blackbody radiation source. Real-time high-resolution videos of the experimental process were observed and recorded through a high-definition (HD) digital camera (Canon 5D Mark III) placed perpendicular to the sample surface to detect the side view of the sample.

B. Optical diagnostic system

Figure 4 also presents an overview of the optical setup, including the OES and LAS systems. The OES system was designed to collect the radiation of reaction products adjacent to the material surface, and the line-of-sight was perpendicular to the centerline of the plasma flow. The system consists of a light collection system, optical fibers, and four spectrometers. The light emitted from the reaction zone was collected by a detector (Gigahertz-Optik, LDM-9811). The emission light was transmitted to four spectrometers through optical fibers equipped behind the camera. The first spectrometer (Ocean Optics, QE65 Pro) equipped with a charge-coupled device camera (1044×64 pixels), recorded spectra over a wide wavelength range of 200–1100 nm. The other three spectrometers (Avantes, AvaSpec-UL2048CL-RS-EVO) monitor finer spectra covering 360–400, 400–630, and 600–805 nm, respectively. Intensity calibration was performed using a National Institute of Standards and Technology traceable quartz–tungsten–halogen standard reference lamp (model 63945, Oriel Instruments, Stratford, CT).

The LAS system targeted the absorption line of atomic oxygen at 777.19 nm. As in the OES system, the LAS laser path was aligned perpendicular to the plasma flow and tangential to the sample surface. The LAS diagnostic system consisted of two major sub-assemblies: the laser emission and control assembly (bottom) and detection assembly (top). The emission and control assembly side included a distributed Bragg reflector (DBR) laser (Photodigm, PH778DBR020BF) driven by a commercial laser controller (Thorlabs, model ITC-502) through temperature and current control. To cover the wavelength range near 777.19 nm, the current of the DBR laser was modulated by a ramp signal of 500 Hz produced by a function generator (Tektronix, AFG-3101). The laser beam was then transmitted and split into two beams through single-mode optical fibers (Thorlabs, P3-780PM-FC-5). The first beam was detected by a Fabry–Pérot interferometer (Thorlabs, F-PSA200-6A-1, 1.5 GHz FSR) to calibrate the absolute wavelength. The other beam was directed to the reaction zone adjacent to the sample surface through a quartz window. The accurate location of surface detection was achieved through displacement control using optical moving stages. On the detection assembly side, a narrow band filter (NBF) with 10 nm width (Thorlabs, FL780–10) was placed before the detector to reduce unwanted plasma emission. The transmitted laser beam was finally collected by two channels of the photodetector. The detected signals were then transmitted to the analysis system through BNC cables and analyzed with the acquisition rate of 200 kHz.

C. Material samples

In this study, SiC was chosen because it is a promising material for TPS design, and quartz was tested as a reference material because of its low catalytic behavior. All the material samples were designed with the same exposed geometry, which featured a body diameter of 50 mm, depth of 30 mm, and leading-edge corner radius of 8 mm. The bottom part with 15 mm diameter and 40 mm length was used for insertion into a water-cooled holder. Figure 5(a) illustrates the sample geometry with the key dimensions, flow direction, and stagnation line coinciding with the plasma flow. The corresponding photos of the samples are shown in Fig. 5(b). The mechanical properties and elemental compositions of SiC were tested before tests. The results showed that the volume density of the SiC ceramics was 3.03 ± 0.01 g/cm^3 and its porosity was less than 1%, indicating a pycnomorphic surface. This also showed that silicon and carbon were the main elements in the ceramics, including 88.6% mass fraction of SiC and 10.7% mass fraction of free silicon (probably introduced by the manufacturing procedure). Additionally, SEM and EDS microscopic inspections on sample surfaces are performed using GeminiSEM 300 from Zeiss, and details will be discussed in Sec. IV D.

IV. RESULTS AND DISCUSSION

A. Visual inspection and surface temperature

Videos of the test sample exposed to the plasma flow were recorded to present visual observation of the sample surface. Snapshots from the HD video at time interval of 20 s are shown in Fig. 6 and compared with the surface temperature history detected every 0.1 s. Because the camera operating mode automatically adjusted the exposure to the variation of light intensity, the brightness differences between each frame cannot be directly correlated with the temperature. Nevertheless, the images still clearly show the heating progress over the sample surface, and the brightness pattern distributions within each image illustrates the temperature gradient around and within the sample.[56] The brightness of the SiC sample [Fig. 6(a)] changes significantly during heating process. The image shows that a small bright spot appears at the stagnation point at around 40 s. As plasma heating continues, the whole light intensity increases sharply and the spot becomes brighter. For the quartz sample, the brightness changes slightly during the whole processes [Fig. 6(c)].

The temperature history in Fig. 6(b) shows a steady flow established after 4 s of the wind tunnel operation. The test sample is then inserted into the plasma flow. For both SiC and quartz material, insertion of the sample into the high-enthalpy flow leads to a natural rise in surface temperature. The surface temperature of the SiC sample (red line) starts to rise sharply at around 20 s. When the plasma exposure time reaches 40 s, the increase rate of the surface temperature suddenly slows down but the temperature keeps increasing to 1600 K at the end of the heating. The blue line represents the temperature variations of the quartz sample. This temperature rises and stabilizes at 1300 K in the first 20 s. During the remaining exposure time, the surface temperature slightly increases and finally reaches approximately 1350 K. Both samples are finally removed from the flow when the exposure time reaches 92 s, leading to a steep drop in surface temperature.

All the samples retained their mechanical integrity after testing with minimal dimensional and mass changes. Figure 7 reveals significant surface changes in test samples after exposure to plasma. All the test samples survived the plasma exposures with minimal dimensional

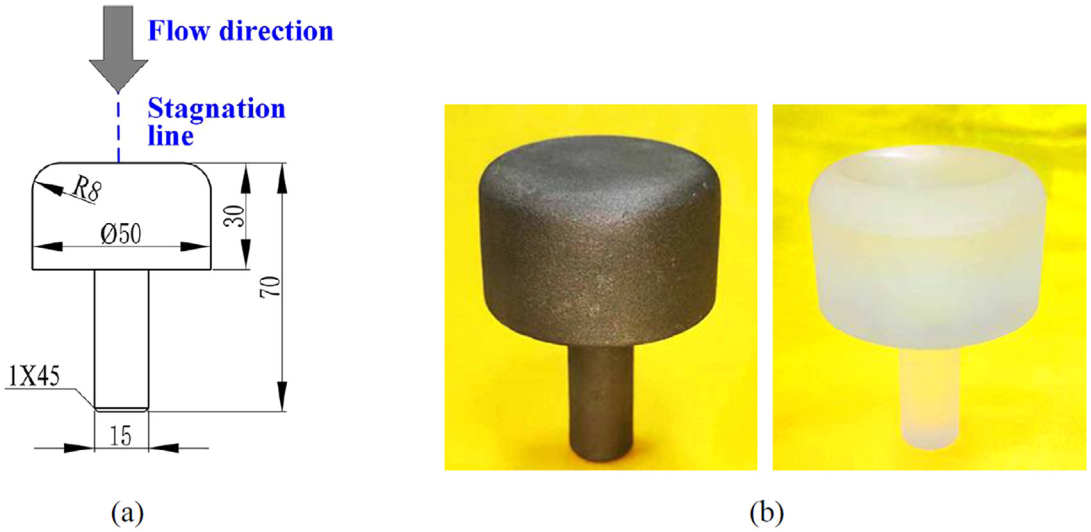

FIG. 5. Sample geometry and visual appearance: (a) schematic and (b) photos for SiC (left) and quartz (right).

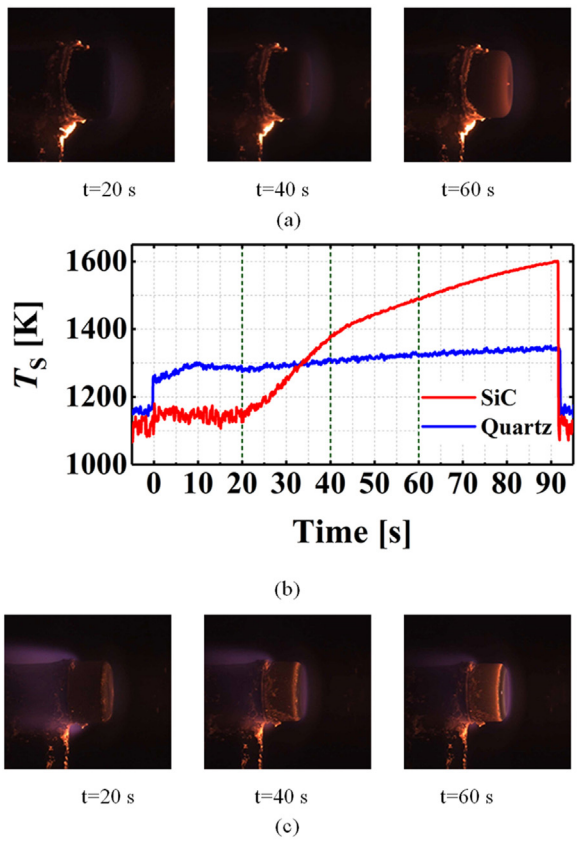

FIG. 6. HD video images showing with temperature variations: (a) Images for SiC at 20 s (left), 40 s (middle), and 60 s (right); (b) surface temperature; (c) images for quartz at 20 s (left), 40 s (middle), and 60 s (right).

and mass changes. Post-test of SiC material [Fig. 7(b)] shows a rough surface with a plenty of bubbles on a macroscopic scale, a white glassy layer, and clear traces of melted products. Such phenomena indicate the formation of an oxidization layer on SiC surface. Details will be discussed in Sec. IV. Visual inspections of quartz sample [Fig. 7(a)] show that the post-test surface is smoother and shinier than the original surface. This provides a higher transmissivity to allow much more light to pass through the material.

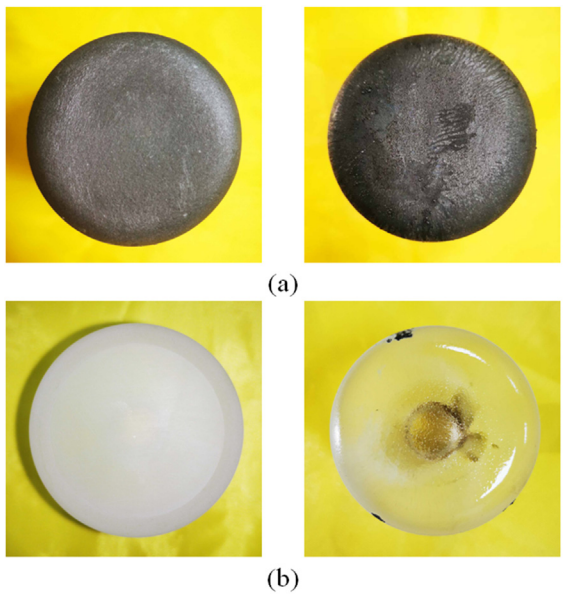

FIG. 7. Visual inspections: (a) pre- (left) and post-test (right) SiC and (b) pre- (left) and post-test (right) quartz.

B. Optical emission spectroscopy

1. Emission spectra

Emission spectroscopic measurements adjacent to the stagnation point of samples open the path to further analysis. Figure 8 shows individual emission spectra extracted at 60 s after insertion for species clarification. In Fig. 8(a), sharp emission lines from atomic oxygen (O) and nitrogen (N) are identified for both materials, which are major components of the dissociated air. Additionally, emission spectra with higher spectral resolution were simultaneously recorded by the other three Avantes spectrometers. Valuable information was found in the ultra violet (UV) range (360–400 nm). For a clearer visualization, emission spectra among this region are illustrated in detail as presented in Fig. 8(b). The red curve plots the emission spectra on SiC sample. The main contributing species in the UV range is the $N_2^+(B^2\Sigma_u^+ \rightarrow X^2\Sigma_g^+)$ first negative system in the 360–400 nm wavelength region,[57] which is excited by the post-shock temperature. The characteristic emission spectra of the quartz sample are dominated by silicon monoxide (SiO) transitions with the bandhead at 383.2 nm and neutral silicon (Si) at approximately 390 nm.[3,58] SiO and Si radiation will be discussed as important reaction species for the quartz surface in Sec. IV B 2.

2. Reaction pathways on the SiC and quartz surfaces

Atomic oxygen was detected on both tested sample surface. The variations in integrated intensity of O (777.19 nm) are plotted in Fig. 9 for further analysis. As the sample is inserted into the plasma, the integrated intensity sharply rises to a peak. This phenomenon relates to the ICP plasma flow properties and the basic OES principles. The air flow has already been dissociated before it reaches the sample surface

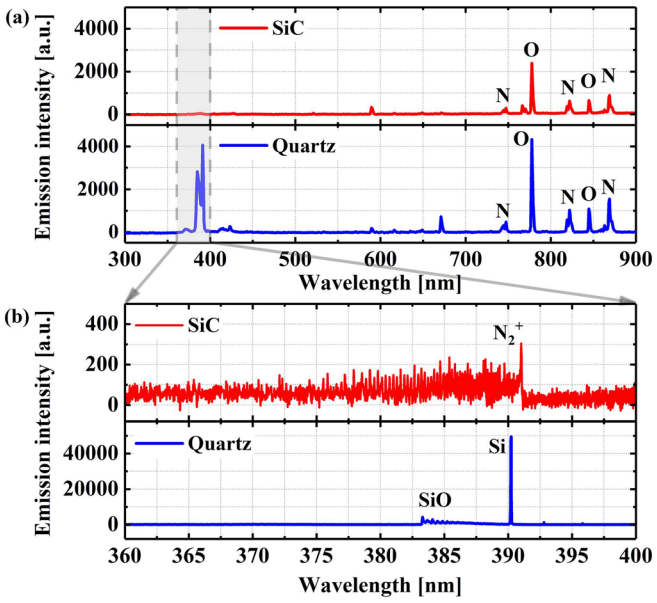

FIG. 8. Emission spectra in arbitrary units 60 s after insertion (red line for the SiC sample, and blue for the quartz sample): (a) Spectra in the wide wavelength range of 300–900 nm and (b) finer spectra in the wavelength range of 360–400 nm.

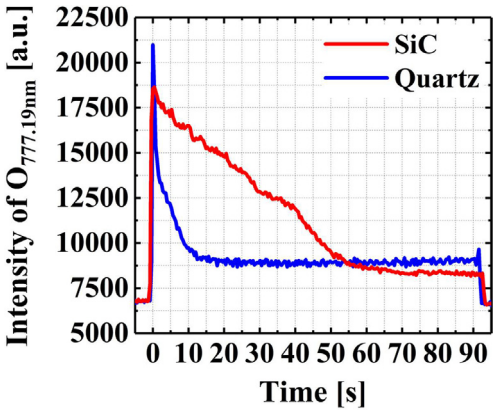

FIG. 9. Dynamic variations of integrated emission intensity of atomic oxygen at 777.19 nm.

in the ICP wind tunnel, which is different from the real flight. As the sample is inserted, the total atomic number density has a minor change compared to that of electron temperature rise due to bow shock heating. The emission intensity increases monotonically with electron temperature and total number density of the radiator. Consequently, a sharp peak occurs in Fig. 9. As the heating continues, the intensity then attenuates to reach steady emission, which lasts until the end of the run.

The emission intensity of the SiC sample decreases more slowly than that of quartz and finally stabilizes at around 50 s. These time variations together with visual inspection in Fig. 7(a) indicate transient formation of a complex multilayer oxide scale containing a silica-rich glassy outer layer that limits oxide growth.[57] As the sample temperature rises through this regime, the gas by-products of oxidation are quickly emitted out of the inner layer, forming multiple bubbles on SiC surface [visible in Fig. 7(a)]. Under continuous heating by the plasma, liquid SiO_2 permeates the porous oxide layer and seals the surface, and a β-cristobalite layer finally forms on the SiC surface. Inward oxygen transport and consumption are then limited. The emission intensity detected by OES (Fig. 9) gradually decreases and eventually ceases. The material used in our study is a pure silicon-carbide ceramics, and the emission spectra on SiC surface show no SiO (regarded as the discriminant of active oxidation). This indicates that the chemical reactions in this period are passive oxidation.[59] In the last 40 s of plasma heating, catalytic recombination between atomic oxygen becomes dominant on SiC surface, and atomic oxygen adjacent to the surface is dynamically balanced by the incoming flow. Notably, O emission intensity on the SiC surface in this period is evidently lower than that on the quartz surface, which will be discussed in Sec. IV with the LAS results. Given these observations, the surface chemistry can be described as[59–61]

0–50 s (oxidation dominant)

1. $2SiC + 3O_2 \rightarrow 2SiO_2 + 2CO$,
2. $SiC + 3O \rightarrow SiO_2 + CO$.

50–92 s (recombination dominant)

3. $O + O \rightarrow O_2$.

For quartz sample, the emission intensity decreases sharply and quickly stabilizes at approximately 10 s. This indicates that the

chemical property of atomic oxygen is more active on SiC surface than that on the quartz surface. The characteristic spectra of Si and SiO illustrated in Fig. 8 are dominant in the UV region on quartz surface. The temporal emission was evaluated by integrating the emission signal as shown in Fig. 10. The radiance gradually increases during plasma heating. Assuming a Boltzmann distribution of excited states, Si emission and SiO emission increase along with species concentration.[3] There is a free silicon residuals from the initial manufacturing process of the quartz sample.[60] Si sublimates at the surface at this high-temperature environment such that the gas adjacent to the surface consists of Si vapor.[62] This enables the silicon gas to radiate before it is carried away by the flow field. The observed SiO emissions may result from the decomposition of the quartz surface and combination of gas-phase species. In the first 10 s after insertion, the high temperature promotes the decomposition and volatilization of SiO_2 into SiO. The combination of Si and O is the leading reaction in the time period of 10–92 s, leading to a continuous increase in SiO emission intensity. Although the catalytic property is extremely low, catalytic recombination of atomic oxygen should also be considered for the quartz sample. Based on the above experimental observations, the most plausible reaction pathways on the quartz surface are as follows:[59,60]

0–10 s

4. $SiO_2 \rightarrow SiO + 1/2O_2$,
5. $SiO_2 \rightarrow SiO + O$,
6. $SiO_2 + O \rightarrow SiO + O_2$.

10–92 s

7. $Si + O \rightarrow SiO$,
8. $O + O \rightarrow O_2$.

C. Laser absorption spectroscopy

1. Data processing and results

Figures 11(a) and 11(b) represent LAS raw data trace detected adjacent to sample surface (x = 0 mm) and 1 mm above the surface (x = 1 mm), respectively. The plasma reaches to a steady state in the first 4 s. At x = 0 mm, part of the laser beam is blocked by the sample surface, leading to an abrupt drop in the laser intensity. Note that the intensity peak of the transmitted laser beam gradually increases during plasma heating, and the baseline of the scanning signal also increases slightly with time. This may relate to surface recession caused by material ablation. After approximately 92 s of heating, the sample is pulled out of the flow and the transmitted intensity of the freestream returns to the original level. At x = 1 mm, the laser beam is not affected by the sample surface, and remains steady during the whole process.

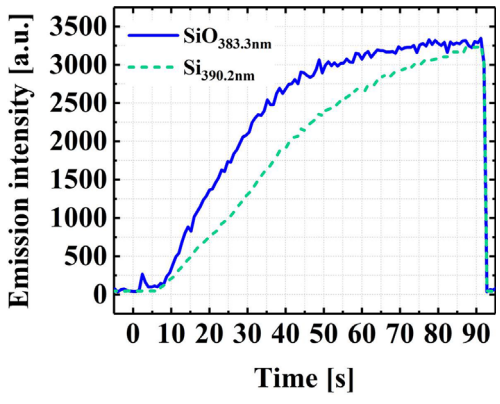

FIG. 10. Dynamic integrated emission intensity of SiO (at 383.3 nm) and Si (at 390.2 nm).

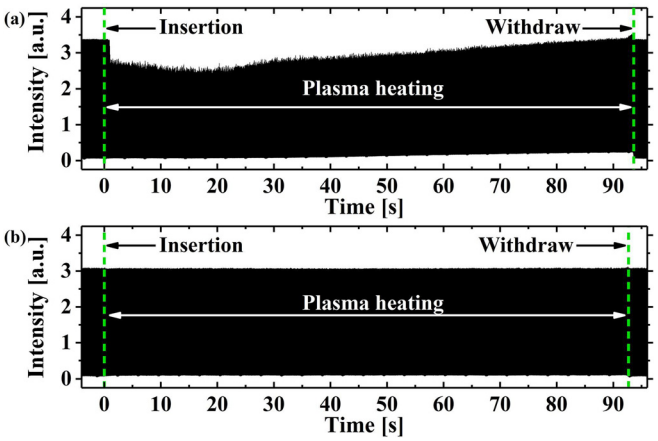

FIG. 11. LAS raw data trace covering the whole experiment processes: (a) locations adjacent to the surface (x = 0 mm) and (b) locations 1 mm above the surface (x = 1 mm).

To accurately obtain the translational temperature and number density of atomic oxygen, sequential scans were averaged to remove stochastic noise from the laser and plume fluctuation. A typical 10-scan averaged signal with high signal-to-noise ratio is shown in Fig. 12(a). A small jump appears near the right side of the absorption peak that is caused by mode hopping of the diode laser. The baseline of the averaged signal is then subtracted and fitted with a Gaussian profile. Figure 12(b) plots a representative absorption peak and its corresponding fitting residual. The fitting residual is smaller than 1% except near the absorption peak, which supports the assumption of Gauss-dominant broadening mechanisms.

The translational temperature T_{tr} of atomic oxygen is directly deduced from the Doppler broadening of the absorption profile,[46,47] and the number density n_O of atomic oxygen is then derived according to Eq. (6). Representative temporally resolved LAS results detected adjacent to the sample surface are presented in Figs. 13(a) (SiC sample) and 13(b) (quartz sample) to show the time history. The starting time of the LAS results represents sample insertion, which is consistent with the OES time history. The steep rise in the translational temperature reflects the aerothermal heating by the bow shock wave. Notably, we oppose translational temperature, and the number density drops deeply at the insertion moment. Such atom consumption closely relates to the basic principle of LAS and the thermochemical process on the sample surface. Different from OES, LAS technique assesses the lower state properties of the targeted species. For our targeted transition at 777.19 nm, the LAS results reflect the number density variations of a metastable state for atomic oxygen. Within the optically thin reaction zone between sample surface and boundary layer, excited atoms are rapidly consumed by complex thermochemical processes,

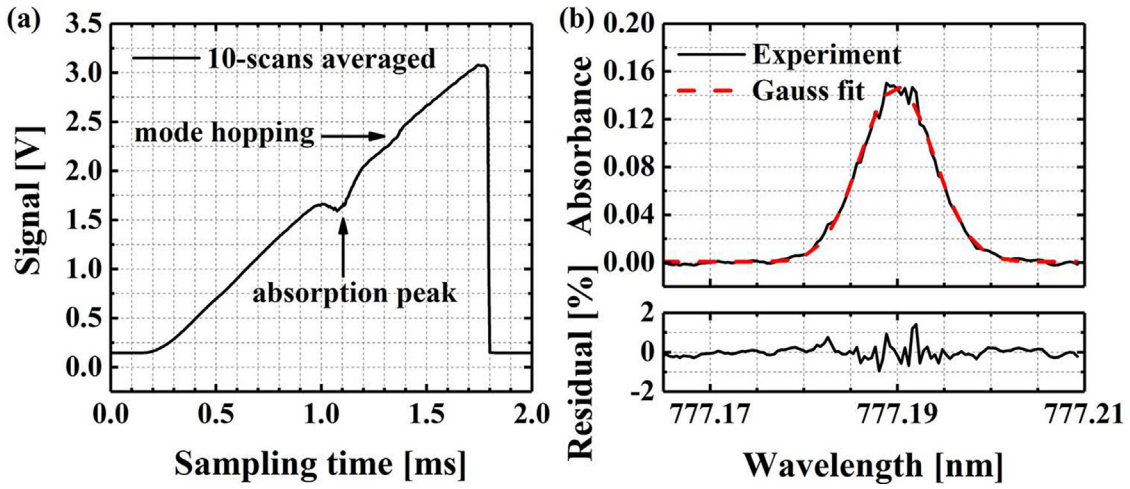

FIG. 12. (a) Representative 50-scans averaged absorption signals. (b) Typical absorption peak after baseline subtraction. Top panel: experimental absorbance spectrum (black solid line) together with its best-fit Gaussian profile (red dashed line). Bottom panel: corresponding Gaussian-fitting residual.

leading to the steep drop in atomic oxygen number density. After the sample withdrawn from the plasma flow, both the translational temperature and number density return to their original levels in the freestream.

2. Relations between n_O and catalytic recombination

Figures 14 and 15 plot the temporally and spatially resolved LAS results for the SiC and quartz samples, respectively. In both figures, the solid and dashed lines represent the LAS results detected adjacent to sample surface (x = 0 mm) and 1 mm above the sample surface, respectively.

Attentions are focused on plasma heating period. First, comparisons are made between different locations for each sample. For SiC sample in Fig. 14, the translational temperature T_{tr} at 1 mm remains steady with slight fluctuations within 100 K. However, T_{tr} at 0 mm varies with time, which closely relates to the surface chemistry. It rises to about 4500 K in the first 30 s, followed by a steep decrease from 30 to 50 s. During the last heating period (50–92 s), T_{tr} increases again and finally stabilizes. These significant changes in temperature reflect the heat release of chemical reactions. The first downward trend indicates that oxidation processes such as exothermic reactions in Sec. IV B are dominant in this period. As the plasma heating continues, oxidized layer forms and gradually covers the sample surface, protecting the surface from deeper oxidation into inner layer. Oxidation gradually ceases and it comes to the second reaction period at around 50 s, where catalytic recombination between atomic oxygen becomes dominant. The chemical heat flux released by recombination enhances the thermal heating on material surface, leading to an increase in T_{tr}. As atomic oxygen is continuously fed by the incoming flow, the SiC surface finally reaches a dynamically steady state, and T_{tr} stables. Interestingly, the variations in the number density n_O correlate well with T_{tr}. Meanwhile, n_O is continuously consumed by oxidation from 0 to 50 s, leading to a downward trend. This behavior is analogous to what is observed in the OES emission intensity (Fig. 9). As the catalytic recombination gradually becomes dominant, n_O reaches a dynamically

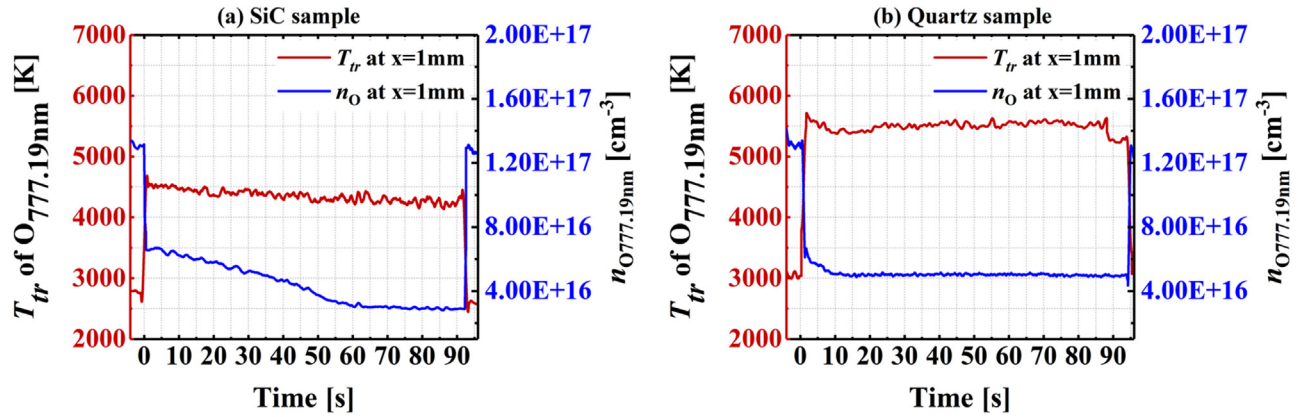

FIG. 13. Representative temporally resolved LAS results adjacent to the surface for the (a) SiC and (b) quartz samples.

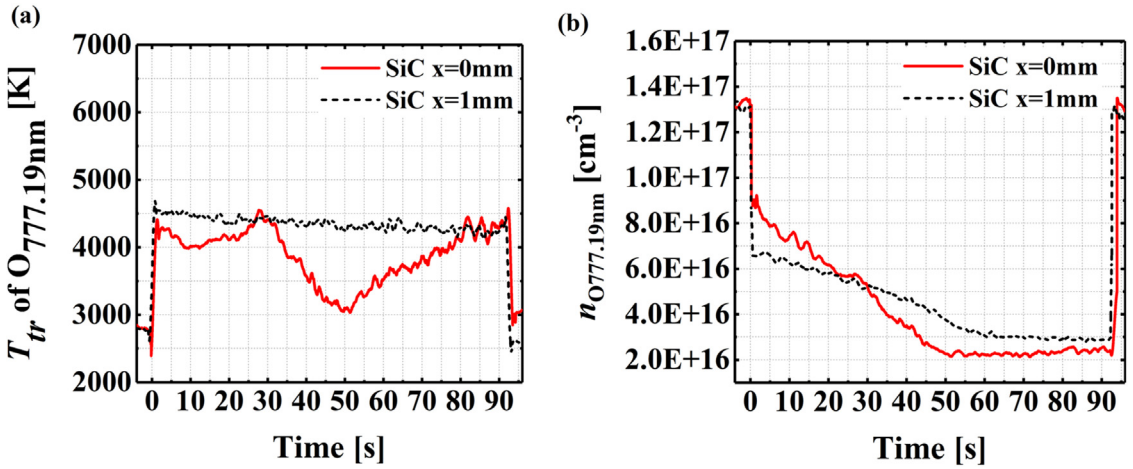

FIG. 14. Temporally and spatially resolved LAS results for the SiC sample: (a) Translational temperature of atomic oxygen at 777.19 nm and (b) number density of atomic oxygen at 777.19 nm.

steady state during the 0–50 s. Notably, both T_{tr} and n_O adjacent to SiC surface (at 0 mm) are lower than that of 1 mm above the surface, showing an axial gradient along the stagnation point. The rapid collisions between dissociated atoms within the boundary layer are believed to enhance the relaxation of translational energy,[63] leading to the T_{tr} axial gradient. The dissociated species diffuse across or flow along the stagnation line to the wall and are finally consumed by chemical reactions, leading to number density gradients.[12]

The quartz surface shows discernible differences in Fig. 15. Both T_{tr} and n_O remain nearly steady throughout plasma heating. Additionally, the axial distributions of these two parameters are nearly constant. Such observations indicate that catalytic recombination causes an n_O axial distributions on the sample surface.

Furthermore, the two materials are also compared at each location. In the period of 50–92 s, the atomic number density on the SiC sample is lower than that on the quartz. This is closely related to catalytic mechanisms within the boundary layer. When dissociated atoms diffuse, impact and are adsorbed on the active site of a highly catalytic material, adsorbed atoms quickly recombine with other atoms to form gas molecules. In such process, the material surface strongly promotes recombination of atoms. The recombination occurs more quickly for materials with higher catalytic property, leading to lower atomic number density. Although the heated SiC surface is partially covered by a layer of β-cristobalite, which has the same chemical formula (SiO_2) as quartz, its catalytic property is higher than that of quartz,[25,29] resulting lower O number density in the last heating period. These differences between the T_{tr} and n_O axial distributions on quartz and SiC sample show that the gradients of these parameters are closely related to the material catalytic property. For materials with higher catalytic property such as SiC, the axial distribution experiences a larger decrease to a stagnation point. For materials with lower catalytic property such as quartz, no evident axial distribution is shown.

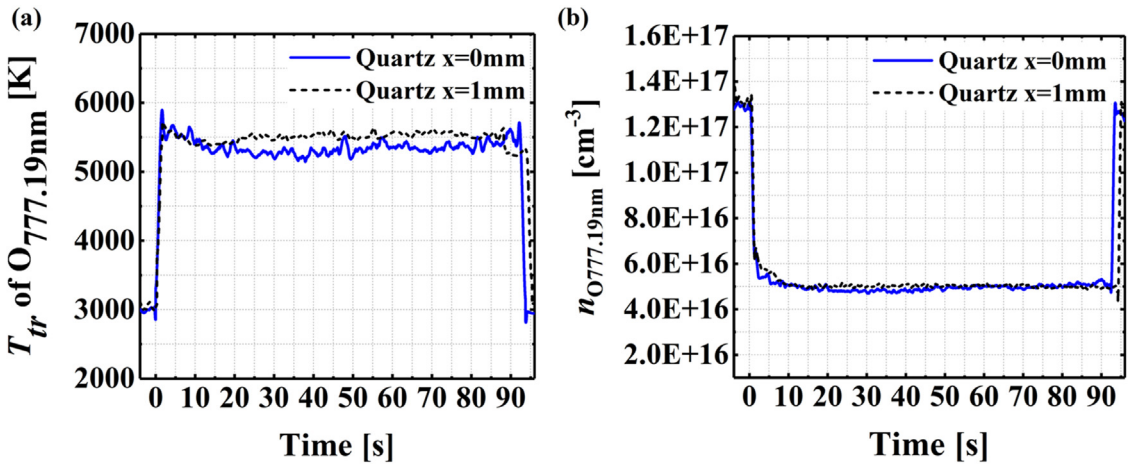

FIG. 15. Temporally and spatially resolved LAS results for the quartz sample: (a) Translational temperature of atomic oxygen at 777.19 nm and (b) number density of atomic oxygen at 777.19 nm.

D. Visual inspection by SEM/EDS

SEM inspection and EDS inspection of material surface provide a visualization of surface changes during plasma exposure, and the results are shown in Figs. 16 for SiC and 17 for quartz. The gray image on the left is the SEM results showing the surface microstructure. Part of the area in the SEM image was chosen to perform EDS. The corresponding EDS results are on the right, showing the element distribution as a white signal on a black background. Though necessarily selective, these images are representative of the surface changes on each test sample.

The SEM micrographs in Fig. 16 show that surface morphology changes significantly after the plasma exposure. The virgin SiC surface is nearly fully dense with limited residual porosity, and the linear pit on the SEM image is mechanical traces left by the cutting procedure. At the same magnification, the post-test surface is inhomogeneous with clearly visible bubbles and holes. Most of the surface is covered by a glassy coating, which appears as a thin film with many small, patchy regions of exposed fragments. There are significant changes to the element distributions and mole fractions according to the EDS maps. The mole fractions of Si and C drop from 48.9 and 48.5 to 34.3 and 30.5 mol. %, respectively. Meanwhile, O element increases notably from 1.8 to 29.9 mol. %. Each element has a well-dispersed distribution before tests, but differences occur on the post-test surface. The Si mole fraction is higher in the pitting on SiC surface than in the rest of the glassy layer. Interestingly, atomic O has a lower mole fraction in the pitting region. These observations prove that oxidation occurs on the sample surface during plasma heating.

In Fig. 17, the microstructure on the virgin surface is flat and grainy, while on the post-test surface, the grainy microstructures have disappeared, but shallow hollows of different sizes have emerged. Note that the small particles in the post-test SEM image do not originate from the material, but are gold grains introduced in the coating process. The EDS images show that Si and O elements have uniform distributions on both the original and post-test surfaces. For the original surface, the mole fractions of element Si (27.4 mol. %) and O (46.5 mol. %) correlate with the chemical formula SiO_2. These changes to 35.9 mol. % Si and 38.0 mol. % O for the post-test surface. This may be caused by the chemical reactions in Sec. IV B. Sample characterization by SEM and EDS directly shows the morphological changes caused by surface reactions, proving the reliability of OES and LAS diagnosis.

V. CONCLUSIONS

An optical diagnostic method based on OES and LAS was used to investigate gas–surface interactions in an aerothermal environment. Experiments were performed in the 1.2 MW inductively coupled plasma wind tunnel at the CAAA at with an enthalpy of 20 MJ/kg and a heating time of 100 s. The characteristic TPS material SiC was tested together with the reference material quartz. OES was used to record the transient reaction products in the reactive flow, which helped to figure out reaction pathways on material surface. Temporally and spatially resolved translational temperature and number density of atomic oxygen at 777.19 nm were quantified by LAS technique. Analyzing the results found that the atomic oxygen number density adjacent to the surface decreases for a material with higher catalytic property (SiC),

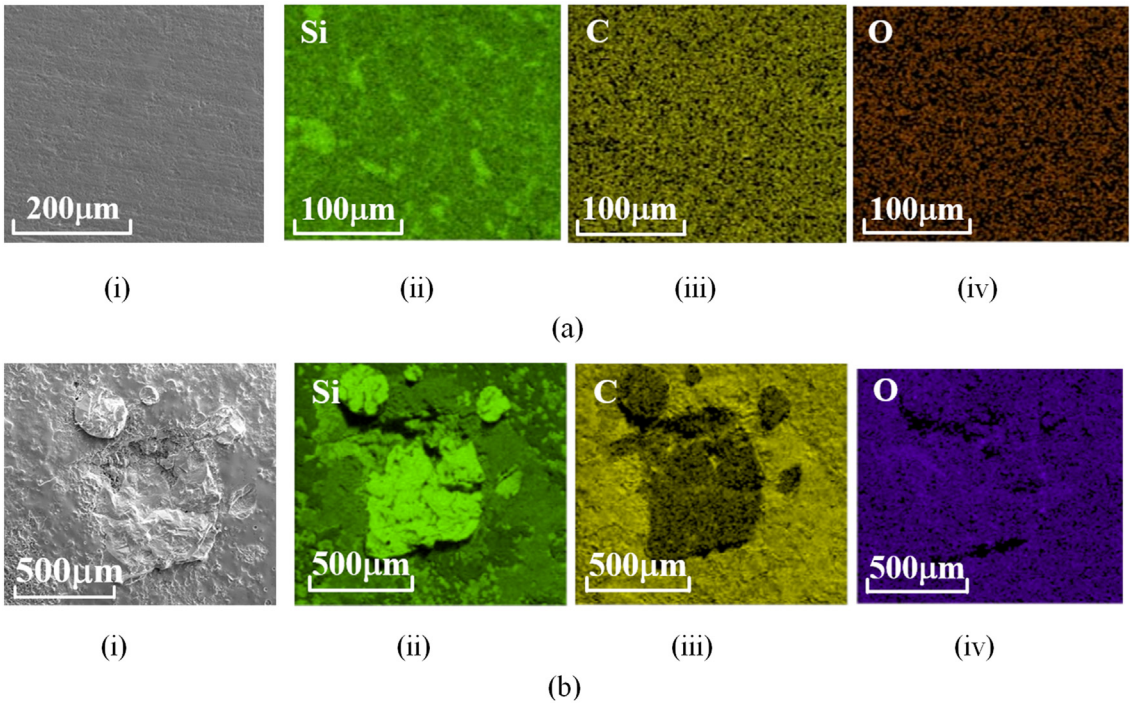

FIG. 16. SEM and EDS images of the SiC sample: (a) Virgin: SEM image (i), EDS maps of Si, C, and O, respectively (ii)–(iv); (b) post-test: SEM image (i), EDS maps of Si, C, and O (ii)–(iv), respectively.

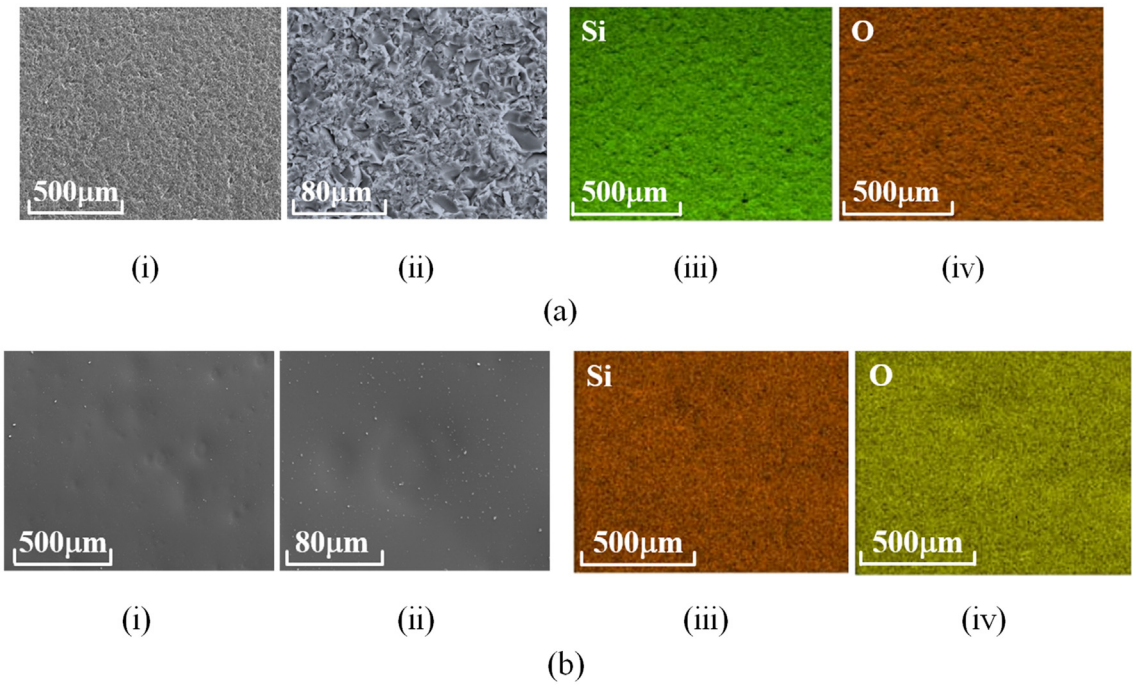

FIG. 17. SEM and EDS images of the quartz sample: (a) Virgin: SEM images at two magnifications (i) and (ii), EDS maps of Si and O (iii) and (iv), respectively; (b) post-test: (i) and (ii) SEM images at two magnifications, (iii) and (iv) EDS maps of Si and O, respectively.

and its axial gradient becomes greater than that with lower catalytic property (quartz). General measurements such as surface temperature, SEM, and OES were also done. We found significant differences between SiC and quartz sample. The optical diagnostic results in this study show that OES and LAS technique are promising for gas–surface interactions research on TPS surface.

Further research will add more diagnostic species such as CO in the UV region to provide more information of the reacting flow. Additionally, characteristic materials such as C/SiC and ZrB_2-SiC will be tested in an ICP wind tunnel, helping further investigations for TPS design. Moreover, numerical simulation should be conducted for a deeper understanding of coupling mechanisms.

ACKNOWLEDGMENTS

This study was financed in part by the National Natural Science Foundation of China (Grant Nos. 11802315, 11927803, 11872368, and 12072355), Key-Area Research and Development Program of Guangdong Province, Grant No. 2021B0909060004, and the Youth Innovation Promotion Association of CAS (Grant No. 2022018).

AUTHOR DECLARATIONS

Conflict of Interest

The authors have no conflicts to disclose.

Author Contributions

Sihan Fang: Conceptualization (equal); Data curation (equal); Investigation (equal); Methodology (equal); Software (equal); Writing – original draft (equal); Writing – review and editing (equal). **Xin Lin:** Data curation (equal); Funding acquisition (equal); Investigation (equal). **Hui Zeng:** Data curation (equal); Investigation (equal). **Xingying Zhu:** Data curation (equal); Investigation (equal). **Fa Zhou:** Investigation (equal). **Junna Yang:** Investigation (equal). **Fei Li:** Funding acquisition (equal). **Dongbin Ou:** Supervision (equal). **Xilong Yu:** Funding acquisition (equal).

DATA AVAILABILITY

The data that support the findings of this study are available from the corresponding authors upon reasonable request.

REFERENCES

[1]D. Stewart, "Determination of surface catalytic efficiency for thermal protection materials—Room temperature to their upper use limit," in 31st Thermophysics Conference, 1996.
[2]D. Stewart and S. Bouslog, "Surface characterization of candidate metallic TPS for RLV," in 33rd Thermophysics Conference, 1999.
[3]F. Panerai, B. Helber, O. Chazot, and M. Balat-Pichelin, "Surface temperature jump beyond active oxidation of carbon/silicon carbide composites in extreme aerothermal conditions," Carbon **71**, 102–119 (2014).
[4]I. Kim, Y. Yang, G. Park, and S. M. Jo, "Catalytic recombination assessment on carbon in dissociated shock tube flow," Acta Astronaut. **181**, 52–60 (2021).
[5]J. W. Streicher, A. Krish, R. K. Hanson, K. M. Hanquist, R. S. Chaudhry, and I. D. Boyd, "Shock-tube measurements of coupled vibration–dissociation time-histories and rate parameters in oxygen and argon mixtures from 5000 K to 10 000 K," Phys. Fluids **32**, 076103 (2020).
[6]J. W. Streicher, A. Krish, and R. K. Hanson, "Vibrational relaxation time measurements in shock-heated oxygen and air from 2000 K to 9000 K using ultraviolet laser absorption," Phys. Fluids **32**, 086101 (2020).

[7]D. G. Fletcher and J. M. Meyers, "Surface catalyzed reaction efficiencies in oxygen plasmas from laser-induced fluorescence measurements," J. Thermophys. Heat Transfer **31**, 410–420 (2017).
[8]Y. Takahashi, R. Nakasato, and N. Oshima, "Analysis of radio frequency blackout for a blunt-body capsule in atmospheric reentry missions," Aerospace **3**, 2 (2016).
[9]H. Luo, A. A. Alexeenko, and S. O. Macheret, "Development of an impulsive model of dissociation in direct simulation Monte Carlo," Phys. Fluids **31**, 087105 (2019).
[10]X. Yang, Y. Gui, W. Tang, Y. Du, L. Liu, G. Xiao, and D. Wei, "Surface thermochemical effects on TPS-coupled aerothermodynamics in hypersonic Martian gas flow," Acta Astronaut. **147**, 445–453 (2018).
[11]B. Massuti-Ballester and G. Herdrich, "Heterogeneous catalysis models of high-temperature materials in high-enthalpy flows," J. Thermophys. Heat Transfer **35**, 459–476 (2021).
[12]A. Anna and I. D. Boyd, "Numerical analysis of surface chemistry in high-enthalpy flows," J. Thermophys. Heat Transfer **29**, 653–670 (2015).
[13]A. N. Molchanova, A. V. Kashkovsky, and Y. A. Bondar, "Surface recombination in the direct simulation Monte Carlo method," Phys. Fluids **30**, 107105 (2018).
[14]B. Massuti-Ballester and G. Herdrich, "Experimental methodology to assess atomic recombination on high-temperature materials," J. Thermophys. Heat Transfer **32**, 353–368 (2018).
[15]J. Thoemel, S. Tirtey, S. Birjmohan, D. Fletcher, and O. Chazot, "Development of an in-flight catalysis experiment within the EXPERT program," in 46th AIAA Aerospace Sciences Meeting and Exhibit, 2008.
[16]C. Park, "Calculation of stagnation-point heating rates associated with stardust vehicle," J. Spacecr. Rockets **44**, 24–32 (2007).
[17]Z. Cui, J. Zhao, L. He, H. Jin, J. Zhang, and D. Wen, "A reactive molecular dynamics study of hyperthermal atomic oxygen erosion mechanisms for graphene sheets," Phys. Fluids **32**, 112110 (2020).
[18]J.-L. Verant, N. Perron, O. Gerasimova, M. Balat-Pichelin, V. Sakharov, A. Kolesnikov, O. Chazot, and P. Omaly, "Microscopic and macroscopic analysis for TPS SiC material under Earth and Mars reentry conditions," in 14th AIAA/AHI Space Planes and Hypersonic Systems and Technologies Conference, 2006.
[19]S. Pidan, M. Auweter-Kurtz, G. Herdrich, and M. Fertig, "Recombination coefficients and spectral emissivity of silicon carbide-based thermal protection materials," J. Thermophys. Heat Transfer **19**, 566–571 (2005).
[20]G. Herdrich, M. Fertig, D. Petkow, A. Steinbeck, and S. Fasoulas, "Experimental and numerical techniques to assess catalysis," Prog. Aeronaut. Sci. **4849**, 27–41 (2012).
[21]B. Vancrayenest and D. Fletcher, "Ablation of carbonaceous heatshields: Spectroscopic emission survey in a subsonic ICP flow," in 40th Thermophysics Conference, 2008.
[22]K. Oguri, T. Sekigawa, J. Kochiyama, and K. Miho, "Catalycity measurement of oxidation-resistant CVD-SiC coating on C/C composite for space vehicle," Mater. Trans. **42**, 856–861 (2001).
[23]M. Mizuno, T. Suzuki, K. Fujita, and T. Sakai, "Experimental and numerical study of thermal response of ablator in an arc-jet facility," in 45th AIAA Aerospace Sciences Meeting and Exhibit, 2007.
[24]M. Mizuno, K. Ishida, T. Ito, T. Kurotaki, and T. Matsuzaki, "Oxygen recombination coefficient on catalytic surfaces in Ar–O_2 inductively coupled plasma by actinometry," Trans. Jpn. Soc. Aero. Space Sci. **49**, 49–54 (2006).
[25]M. Balat-Pichelin, J. M. Badie, R. Berjoan, and P. Boubert, "Recombination coefficient of atomic oxygen on ceramic materials under earth re-entry conditions by optical emission spectroscopy," Chem. Phys. **291**, 181–194 (2003).
[26]T. Marynowski, S. Löhle, and S. Fasoulas, "Two-photon absorption laser-induced fluorescence investigation of CO_2 plasmas for Mars entry," J. Thermophys. Heat Transfer **28**, 394–400 (2014).
[27]L. Ma, X. Li, S. T. Sanders, A. W. Caswell, S. Roy, D. H. Plemmons, and J. R. Gord, "50-kHz-rate 2D imaging of temperature and H_2O concentration at the exhaust plane of a J85 engine using hyperspectral tomography," Opt. Express **21**, 1152–1162 (2013).
[28]M. J. H. Balat, M. Czerniak, and J. M. Badie, "Ceramics catalysis evaluation at high temperature using thermal and chemical approaches," J. Spacecr. Rockets **36**, 273–279 (1999).
[29]L. Bedra and M. J. H. Balat-Pichelin, "Comparative modeling study and experimental results of atomic oxygen recombination on silica-based surfaces at high temperature," Aerosp. Sci. Technol. **9**, 318–328 (2005).
[30]S. Förster, C. Mohr, and W. Viöl, "Investigations of an atmospheric pressure plasma jet by optical emission spectroscopy," Surf. Coat. Technol. **200**, 827–830 (2005).
[31]O. Samimi-Abianeh, "Line-of-sight optical diagnostic for measuring combustion products using species' natural emissions," Exp. Therm. Fluid Sci. **118**, 110174 (2020).
[32]C. Aragón and J. A. Aguilera, "Characterization of laser induced plasmas by optical emission spectroscopy: A review of experiments and methods," Spectrochim. Acta, Part B **63**, 893–916 (2008).
[33]Q. Y. Zhang, D. Q. Shi, W. Xu, C. Y. Miao, C. Y. Ma, C. S. Ren, C. Zhang, and Z. Yi, "Determination of vibrational and rotational temperatures in highly constricted nitrogen plasmas by fitting the second positive system of N_2 molecules," AIP Adv. **5**, 057158 (2015).
[34]C. Liu and L. Xu, "Laser absorption spectroscopy for combustion diagnosis in reactive flows: A review," Appl. Spectrosc. Rev. **54**, 1–44 (2019).
[35]R. K. Hanson, R. M. Spearrin, and C. S. Goldenstein, *Spectroscopy and Optical Diagnostics for Gases* (Springer International Publishing, 2016).
[36]L. Shao, B. Fang, F. Zheng, X. Qiu, Q. He, J. Wei, C. Li, and W. Zhao, "Simultaneous detection of atmospheric CO and CH_4 based on TDLAS using a single 2.3 μm DFB laser," Spectrochim. Acta, Part A **222**, 117118 (2019).
[37]I. A. Schultz, C. S. Goldenstein, J. B. Jeffries, R. K. Hanson, R. D. Rockwell, and C. P. Goyne, "Diode laser absorption sensor for combustion progress in a model scramjet," J. Propul. Power **30**, 550–557 (2014).
[38]C. S. Goldenstein, R. M. Spearrin, J. B. Jeffries, and R. K. Hanson, "Infrared laser absorption sensors for multiple performance parameters in a detonation combustor," Proc. Combust. Inst. **35**, 3739–3747 (2015).
[39]K. Kunze, M. Miclea, G. Musa, J. Franzke, C. Vadla, and K. Niemax, "Diode laser-aided diagnostics of a low-pressure dielectric barrier discharge applied in element-selective detection of molecular species," Spectrochim. Acta, Part B **57**, 137–146 (2002).
[40]H. Burghaus, C. F. Kaiser, A. S. Pagan, S. Fasoulas, and G. Herdrich, "Aerothermodynamic characterization of an inductively generated CO_2 plasma by laser absorption spectroscopy," in AIAA SCITECH 2022 Forum, 2021.
[41]M. Nations, L. S. Chang, J. B. Jeffries, R. K. Hanson, M. E. MacDonald, A. Nawaz, J. S. Taunk, T. Gök ç en, and G. Raiche, "Characterization of a large-scale arcjet facility using tunable diode laser absorption spectroscopy," AIAA J. **55**, 3757–3766 (2017).
[42]C. Penache, M. Miclea, A. Br uning-Demian, O. Hohn, S. Sch ssler, T. Jahnke, K. Niemax, and H. Schmidt-B cking, "Characterization of a high-pressure microdischarge using diode laser atomic absorption spectroscopy," Plasma Sources Sci. Technol. **11**, 476–483 (2002).
[43]M. Nations, S. Wang, C. S. Goldenstein, K. Sun, D. F. Davidson, J. B. Jeffries, and R. K. Hanson, "Shock-tube measurements of excited oxygen atoms using cavity-enhanced absorption spectroscopy," Appl. Opt. **54**, 8766–8775 (2015).
[44]R. Smith, D. Wagner, and J. Cunningham, "A survey of current and future plasma arc-heated test facilities for aerospace and commercial applications," in 36th AIAA Aerospace Sciences Meeting and Exhibit, 1998.
[45]M. Matsui, "Application of laser absorption spectroscopy to high enthalpy flow diagnostics," Ph.D. thesis (Department of Advanced Energy Engineering, Tokyo, 2005).
[46]H. Tajayanagi, C. Bauer, H. Osawa, T. Suzuki, and K. Fujita, "Translational temperature distribution in an inductively coupled plasma flow for catalytic efficiency measurements," Trans. Jpn. Soc. Artif. Intell. Aerosp. Technol. Jpn. **8**, 1 (2011).
[47]M. Matsui, K. Komurasaki, G. Herdrich, and M. Auweter-Kurtz, "Laser absorption spectroscopy in inductive plasma generator flows," in 42nd AIAA Aerospace Sciences Meeting and Exhibit, 2004.
[48]M. Matsui, K. Komurasaki, and Y. Arakawa, "Sensitivity enhancement of laser absorption spectroscopy for atomic oxygen measurement in microwave air plasma," Vacuum **83**, 21–24 (2008).
[49]M. Auweter-Kurtz, G. Herdrich, T. Laux, and K. Komurasaki, "Probe measurements and laser absorption spectroscopy on the IRS IPG3 plasma plume," in 35th AIAA Thermophysics Conference, 2001.

[50]M. Matsui, K. Komurasaki, and Y. Arakawa, "Laser absorption spectroscopy in high enthalpy flows," in 38th AIAA Thermophysics Conference, 2005.
[51]C. O. Laux, T. G. Spence, C. H. Kruger, and R. N. Zare, "Optical diagnostics of atmospheric pressure air plasmas," Plasma Sources Sci. Technol. **12**, 125–138 (2003).
[52]M. De Cesare, L. Savino, G. Ceglia, D. Alfano, F. D. Carolo, A. D. French, D. Rapagnani, S. Gravina, A. Cipullo, A. Del Vecchio, A. Di Leva, A. D'Onofrio, U. Galietti, L. Gialanella, and F. Terrasi, "Applied radiation physics techniques for diagnostic evaluation of the plasma wind and thermal protection system critical parameters in aerospace re-entry," Prog. Aeronaut. Sci. **112**, 100550 (2020).
[53]C. Park, R. L. Jaffe, and H. Partridge, "Chemical-kinetic parameters of hyperbolic earth entry," J. Thermophys. Heat Transfer **15**, 76–90 (2001).
[54]A. Tibere-Inglesse, "Radiation of nonequilibrium recombining plasma flows," Ph.D. thesis (Université Paris-Saclay, 2019).
[55]A. Viladegut and O. Chazot, "Catalytic characterization in plasma wind tunnels under the influence of gaseous recombination," Phys. Fluids **34**, 027108 (2022).
[56]B. Helber, A. Turchi, J. B. Scoggins, A. Hubin, and T. E. Magin, "Experimental investigation of ablation and pyrolysis processes of carbon-phenolic ablators in atmospheric entry plasmas," Int. J. Heat Mass Transfer **100**, 810–824 (2016).
[57]D. Fletcher, J. Marschall, W. Fahrenholtz, G. Hilmas, and S. Zhu, "Optical emission spectroscopy during plasmatron testing of ZrB_2–SiC ultrahigh-temperature ceramic composites," J. Thermophys. Heat Transfer **23**, 279–285 (2009).
[58]W. Marine, V. Tokarev, M. Gerri, M. Sentis, and E. Fogarassy, "Ablation dynamics of silicon based targets in oxygen and nitrogen atmospheres," Thin Solid Films **241**, 103–108 (1994).
[59]M. A-K. Georg Herdrich, M. Fertig, S. Löhle, and S. Pidan, "Catalytic and oxidative behaviour of silicon carbide based materials for thermal protection materials," in 55th International Astronautical Congress, 2004.
[60]H. Hald, "Operational limits for reusable space transportation systems due to physical boundaries of C/SiC materials," Aerosp. Sci. Technol. **7**, 551–559 (2003).
[61]W. P. Owens, J. M. Meyers, and D. G. Fletcher, "Surface catalyzed recombination efficiencies for flexible thermal protection materials in air plasma," in 44th AIAA Thermophysics Conference, 2013.
[62]P. S. Grinchuk, M. S. Tretyak, and V. V. Chuprasov, "Thermal protection material on the base of silicon-carbide ceramics," IOP Conf. Ser: Mater. Sci. Eng. **709**, 044112 (2020).
[63]S.-H. Park, J. Navarro Laboulais, P. Leyland, and S. Mischler, "Re-entry survival analysis and ground risk assessment of space debris considering by-products generation," Acta Astronaut. **179**, 604–618 (2021).